Supplementary information for

Direct observation of ion cyclotron damping of turbulent energy in Earth's magnetosheath plasma

August 4, 2024

A. S. Afshari, G. G. Howes, J. R. Shuster, K. G. Klein, D. McGinnis, M. M. Martinović, S. A. Boardsen, C. R. Brown, R. Huang, D. P. Hartley, C. A. Kletzing

Corresponding author: arya-afshari@uiowa.edu

S1. Linear Kinetic Theory Prediction of Velocity-Space Signatures of Ion Cyclotron Damping

Here we present an explanation of the velocity-space signatures for ion cyclotron damping of an Alfvén/ion cyclotron wave using the self-consistently determined wave eigenfunction using the `PLUME` linear Vlasov-Maxwell dispersion relation solver [s1], which predicts the complex eigenfrequency $\omega + i\gamma$ given the wavevector and plasma parameters. We choose a fiducial case of a fully ionized, hydrogenic plasma with isotropic Maxwellian ion and electron velocity distributions and plasma parameters $\beta_i = 1$, $T_i/T_e = 1$, $v_{ti}/c = 10^{-4}$, and $m_i/m_e = 1836$. In Fig. S1, for the Alfvén/ion cyclotron wave with wavevector $\mathbf{k} = k_\perp \hat{\mathbf{e}}_{\perp 1} + k_\parallel \hat{\mathbf{e}}_\parallel$, we present (a) the normalized real wave frequency ω/Ω_i (black) compared to an analytical approximation (red dashed) inspired by the cold plasma ion cyclotron wave dispersion relation [s2, s3],

$$\frac{\omega}{\Omega_i} = \frac{k_\parallel d_i}{2} \left(\frac{v_{A*}}{v_A}\right) \left[\sqrt{(k_\parallel d_i)^2 (v_{A*}/v_A)^2 + 4} - (k_\parallel d_i)(v_{A*}/v_A)\right]^{1/2} \tag{S1}$$

with a correction for the phase speed of the Alfvén wave due to pressure anisotropy v_{A*} relative to the standard Alfvén speed

$$\frac{v_{A*}}{v_A} = \left[1 + \sum_s \frac{\beta_{\parallel s}}{2} \left(\frac{T_{\perp s}}{T_{\parallel s}} - 1\right)\right]^{1/2}. \tag{S2}$$

Note that, at large scales where $k_\parallel d_i \ll 1$, a temperature anisotropy with $T_{\perp s}/T_{\parallel s} > 1$ increases the wave phase velocity and $T_{\perp s}/T_{\parallel s} < 1$ decreases the phase velocity relative to the Alfvén velocity v_A in an isotropic pressure plasma. Here $d_i = c/\omega_{pi} = v_A/\Omega_i$ is the usual definition of the ion inertial length, where c is the speed of light, $\omega_{pi} = \sqrt{n_i q_i^2/(\epsilon_0 m_i)}$ is the ion plasma frequency, and $\Omega_i = q_i B_0/m_i$ is the ion cyclotron frequency. We see that the analytical approximation for the frequency is accurate up to $k_\parallel d_i \lesssim 0.3$, where the damping is weak with $-\gamma/\omega < 0.1$.

In Fig. S1(b), we plot the normalized total collisionless damping rate $-\gamma/\omega$ (black dashed) for $k_\perp d_i = 10^{-2}$ over a range $10^{-2} \le k_\parallel d_i \le 10$. In addition, we also show in (b) the total normalized ion damping rate γ_i/ω (thin red) and total normalized electron damping rate γ_e/ω (thin blue) are plotted, showing clearly that the total damping rate for this ion cyclotron wave (ICW) is dominated by the ions. Furthermore, the contributions to the collisionless damping on the ions are calculated separately, showing at $k_\parallel d_i \lesssim 0.2$ nearly equal contributions from ion Landau damping $\gamma_{i,LD}$ (red short dashed) and ion transit-time damping $\gamma_{i,TTD}$ (red long dashed); at $k_\parallel d_i \gtrsim 0.2$, ion cyclotron damping $\gamma_{i,CD}$ (green dashed) becomes the dominant collisionless

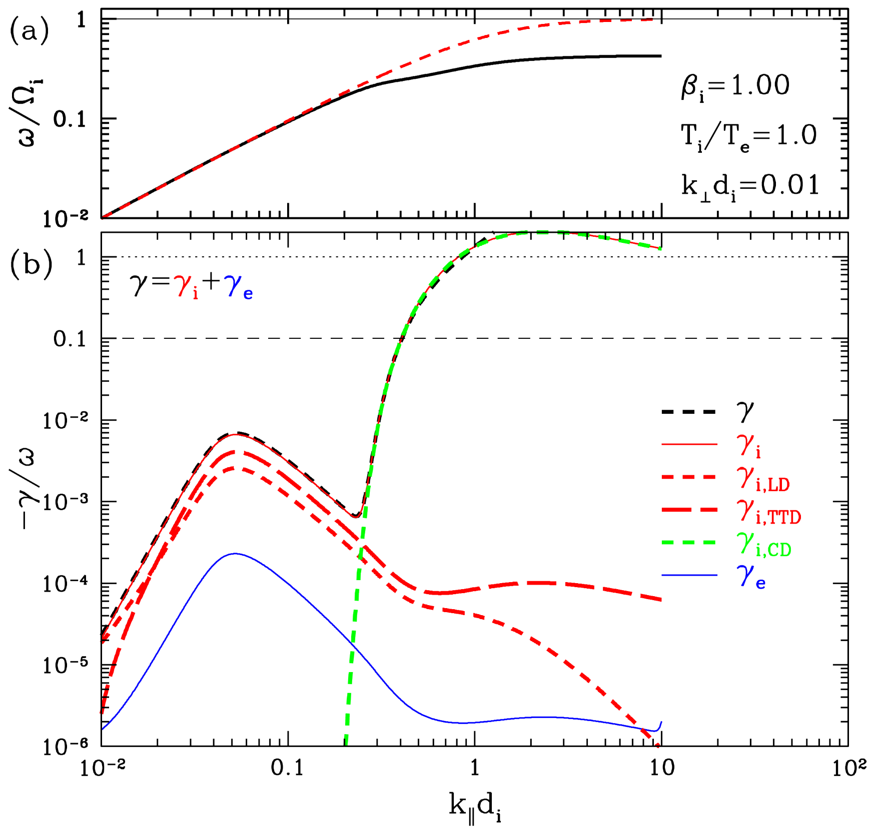

Figure S1: **Frequency and damping rate of Alfvén/ion cyclotron wave.** In a Maxwellian plasma with $\beta_i = 1$, $T_i/T_e = 1$, $v_{ti}/c = 10^{-4}$, and $m_i/m_e = 1836$, we plot (a) the normalized frequency ω/Ω_i (black) and the analytical approxmation by eq. (S1) (red dashed) and (b) normalized total collisionless damping rate γ/ω (black dashed) for $k_\perp d_i = 10^{-2}$ over a range $10^{-2} \leq k_\parallel d_i \leq 10$. Separate contributions to the total collisionless damping rate γ/ω (black dashed) are shown: total ion damping γ_i (thin red); total electron damping rate γ_e (thin blue); ion Landau damping $\gamma_{i,LD}$ (red short dashed); ion transit-time damping $\gamma_{i,TTD}$ (red long dashed); and ion cyclotron damping $\gamma_{i,CD}$ (green dashed).

damping mechanism. Significant damping rates with $-\gamma/\omega \gtrsim 0.1$ occur for $k_\parallel d_i \gtrsim 0.4$, where ion cyclotron damping dominates.

To predict the velocity-space signatures of ion cyclotron damping in the perpendicular velocity space $(v_{\perp 1}, v_{\perp 2})$, we employ the analytical model given by (6) and (7) in the manuscript with the complex phase and amplitude relationships for the perpendicular components of the electric field and ion fluid velocity derived directly from the linear eigenfunctions calculated by the `PLUME` solver. For this calculation, we choose a wave amplitude given by $E_{\perp 1}/(v_A B_0) =$

0.3. In Fig. S2, we plot the perpendicular velocity-space signatures $C_{E_{\perp 1}}(v_{\perp 1}, v_{\perp 2})$ (left column) and $C_{E_{\perp 2}}(v_{\perp 1}, v_{\perp 2})$ (right column) for the ICW from Fig. S1 with $k_\parallel d_i = 0.4$ (top row), $k_\parallel d_i = 0.8$ (middle row), and $k_\parallel d_i = 1.2$ (bottom row). Note that these predicted velocity-space signatures are time-averaged over one full period of the ICW, thus they contain the net effect of the work done by the perpendicular electric field on the ions. In all cases, we observe quadrupolar signatures dominated by energy transfer to the ions (red), with an increasing skew to the quadrupolar pattern with increasing $k_\parallel d_i$, which arises from the phase shift between the perpendicular electric field and the perpendicular ion bulk velocity decreasing from nearly out-of-phase with $\delta_1 = \delta_2 = -0.49\pi$ at $k_\parallel d_i = 0.4$ to more in-phase with $\delta_1 = \delta_2 = -0.27\pi$ at $k_\parallel d_i = 1.2$. All cases have $\phi = -0.5\pi$. It is worth noting that the quantitative skew in the pattern provides a potential means to determine the parallel wavenumber of the ICW undergoing damping.

To understand why ion cyclotron damping creates the quadrupolar pattern in perpendicular velocity space $(v_{\perp 1}, v_{\perp 2})$, it is necessary to look at the instantaneous work done by the perpendicular electric field over the full ICW period T. In Fig. S3, we plot the instantaneous field-particle correlation for $C_{E_{\perp 1}}(v_{\perp 1}, v_{\perp 2})$ for the $k_\parallel d_i = 0.8$ case at eight different, equally spaced phases of the wave, parameterized by $t/T = \omega t/2\pi$. In each panel, we plot the mean perpendicular bulk velocity (star) and a circle of radius one thermal velocity $\Delta v_\perp / v_{ti} = 1$ to indicate the ion distribution at that time throughout its circularly polarized orbit. Each case yields a bipolar signature of energization by the $E_{\perp 1}$ component of the electric field. Averaging over the full 2π phase of the ion cyclotron period leads to the quadrupolar signature seen in Fig. S2(c), where the energization of the ions is dominated by positive (red) transfer to the ions in the second and fourth quadrants of that plot.

Note that the total energization of the ions by the perpendicular electric field over perpendicular velocity space is given by the sum of $C_{E_\perp}(v_{\perp 1}, v_{\perp 2}) = C_{E_{\perp 1}} + C_{E_{\perp 2}}$, leading to the total ion energization pattern in perpendicular velocity space $(v_{\perp 1}, v_{\perp 2})$ shown in Fig. S4(a) for the $k_\parallel d_i = 0.8$ case. If the full factor of v^2 in the electric field term of Eq. (1) is used in the definition of the perpendicular field-particle correlation, given by

$$C_{E_\perp s}^{(v^2)}(\mathbf{r}_0, \mathbf{v}, t; \tau) = \frac{1}{\tau} \int_{t-\tau/2}^{t+\tau/2} dt' \frac{-q_s v^2}{2} \left(\frac{\partial f_s(\mathbf{r}_0, \mathbf{v}, t')}{\partial v_{\perp 1}} E_{\perp 1}(\mathbf{r}_0, t') + \frac{\partial f_s(\mathbf{r}_0, \mathbf{v}, t')}{\partial v_{\perp 2}} E_{\perp 2}(\mathbf{r}_0, t') \right), \tag{S3}$$

we obtain the perpendicular field-particle correlation in Fig. S4(b). This alternative version in panel (b) corresponds to an intuitive expectation for ion cyclotron damping in which ions with $v_\perp / v_{ti} < 1$ are accelerated to a perpendicular velocity with $v_\perp / v_{ti} > 1$, generating the red circular pattern with a blue center. Note, however, that, when integrated over velocity space, the

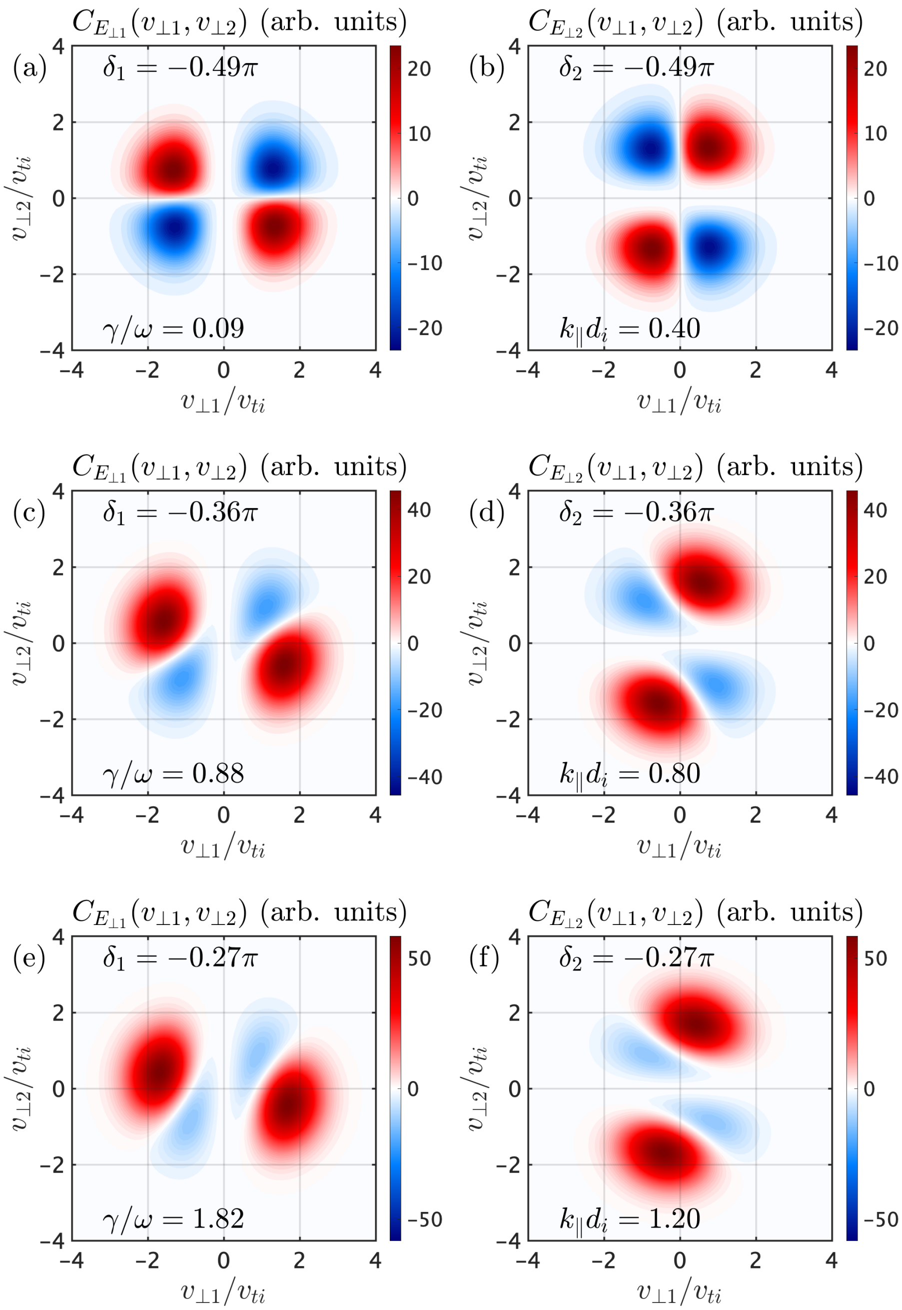

Figure S2: **Velocity-space signatures of ion cyclotron damping**. The perpendicular velocity-space signatures $C_{E_\perp 1}(v_{\perp 1}, v_{\perp 2})$ (left column) and $C_{E_\perp 2}(v_{\perp 1}, v_{\perp 2})$ (right column) for the ion cyclotron wave from Fig. S1 with $k_\parallel d_i = 0.4$ (a,b), $k_\parallel d_i = 0.8$ (c,d), and $k_\parallel d_i = 1.2$ (e,f).

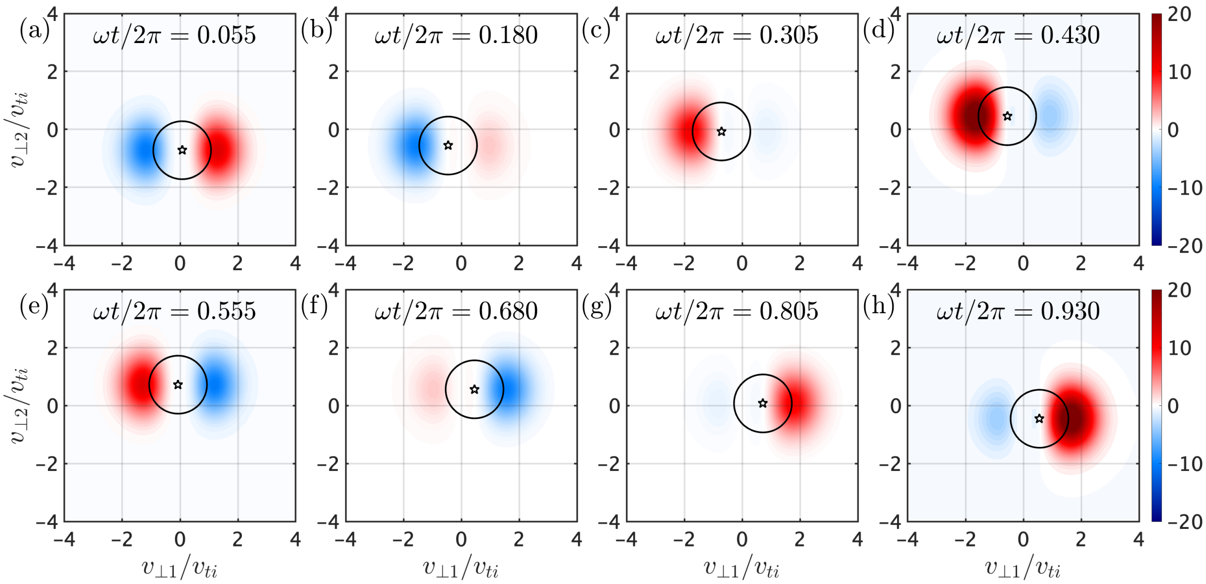

Figure S3: **Instantaneous correlation by phase**. The instantaneous field-particle correlation $C_{E_\perp 1}(v_{\perp 1}, v_{\perp 2})$ in perpendicular velocity space at 8 equally spaced phases of ion cyclotron wave $\omega t/2\pi$. The summed effect over the full 2π phase of the ion cyclotron wave yields the quadrupolar signature seen in Fig. S2(c).

net rate of ion energization is exactly the same in both panels (a) and (b) because, for example, the $v_{\perp 2}^2$ contribution to v^2 yields zero when the correlation is integrated over $v_{\perp 1}$.

It is worthwhile noting here that if the ion velocity distribution is separated into the sum of a steady equilibrium and a time-varying perturbation, $f_i(\mathbf{v}, t) = f_{i0}(\mathbf{v}) + \delta f_i(\mathbf{v}, t)$, then the velocity-space signature of the perpendicular field-particle correlation using the full ion velocity distribution $f_i(\mathbf{v}, t)$ is exactly the same as that using the perturbed ion velocity distribution $\delta f_i(\mathbf{v}, t)$ as long as (i) the correlation is taken over an integral number of wave periods and (ii) the damping rate is weak $-\gamma/\omega \ll 1$ so that the oscillating energy transfer of the undamped wave motion cancels out between the first and second halves of the wave period. Thus, observational field-particle correlations using the full ion velocity distribution $f_i(\mathbf{v}, t)$ can be compared directly to the predictions from field-particle correlation calculations that use the perturbed ion velocity distribution $\delta f_i(\mathbf{v}, t)$.

S2. Ion Cyclotron Wave Modes Driven Unstable by the Alfvén/Ion Cyclotron Instability

In the investigation of the source of the ICW observed to damp in the *MMS* measurements, it is worthwhile to determine what are the typical wave vectors of the modes that may be

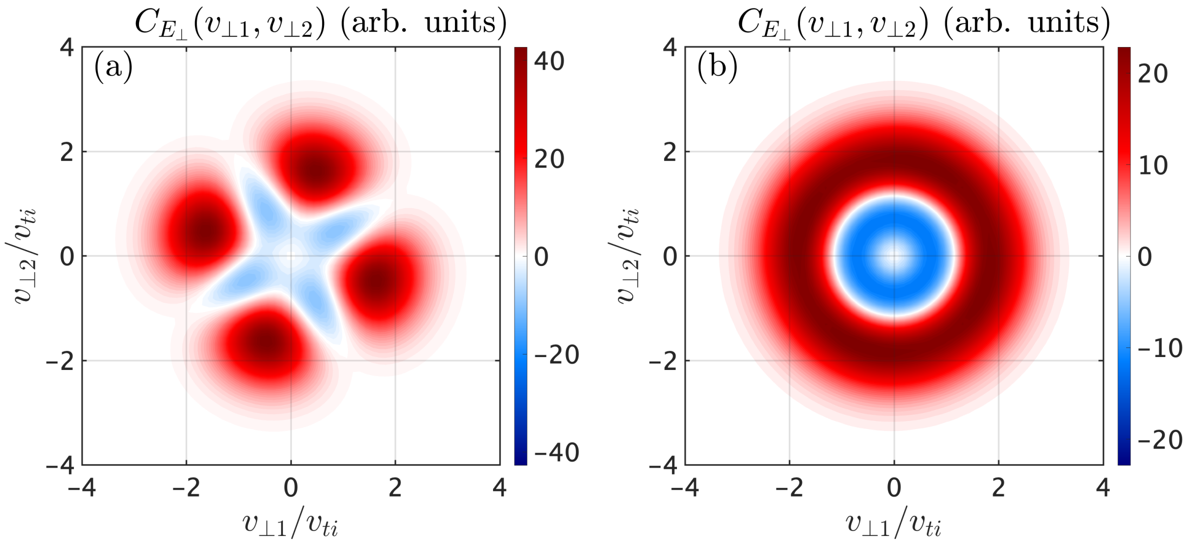

Figure S4: **Total perpendicular velocity-space signature**. (a) $C_{E_\perp}(v_{\perp 1}, v_{\perp 2})$ using the component field-particle correlation defined in Eq. (2) and (b) $C_{E_\perp}^{(v^2)}(\mathbf{r}_0, \mathbf{v})$ using the full v^2 factor in the correlation definition in eq. (S3).

driven unstable by the ion temperature anisotropy. Using the `PLUME` linear Vlasov-Maxwell dispersion relation solver [s1], we compute the growth or damping rates of wave modes over the normalized wavevector[1] range $10^{-2} \leq k_\perp \rho_{\perp i} \leq 10$ and $10^{-2} \leq k_\parallel \rho_{\perp i} \leq 10$, where $\rho_{\perp i} = v_{\perp ti}/\Omega_i = d_i (T_{\perp i}/T_{\parallel i})^{1/2} \beta_{\parallel i}^{1/2}$ and the perpendicular ion thermal velocity is given by $v_{\perp ti}^2 = 2T_{\perp i}/m_i$. We model a fully ionized, hydrogenic plasma with bi-Maxwellian velocity distributions and mass ratio $m_i/m_e = 1836$, and we compute the dimensionless plasma parameters using the *MMS* measurements during the interval: $\beta_{\parallel i} = 0.383$, $T_{\parallel i}/T_{\parallel e} = 6.84$, $T_{\perp i}/T_{\parallel i} = 2.43$, $T_{\perp e}/T_{\parallel e} = 0.973$, and $v_{\parallel ti}/c = 7.34 \times 10^{-4}$, where the parallel ion thermal velocity is given by $v_{\parallel ti}^2 = 2T_{\parallel i}/m_i$. For the Alfvén/ion cyclotron wave mode, the resulting normalized growth rates γ/Ω_i are plotted linearly in the left panel of Fig. S5 and the normalized damping rates $-\gamma/\Omega_i$ are plotted logarithmically in the right panel. It is clear that the measured ion temperature anisotropy leads to unstable growth of the ICWs with $0.3 \lesssim k_\parallel \rho_{\perp i} \lesssim 1.0$ and $k_\perp < k_\parallel$; for the most rapidly growing modes, the unstable wave vectors are predominantly

[1]Note that the ion thermal Larmor radius $\rho_{\perp i}$ is the natural length scale to normalize $k_\perp$, and we choose to normalize $k_\parallel$ by the same characteristic length so the wavevector anisotropy $k_\parallel/k_\perp$ of a wave mode is immediately evident from the plot. Choosing a parallel wavevector normalization of $k_\parallel d_i$ would include scalings of $T_{\perp i}/T_{\parallel i}$ and $\beta_{\parallel i}$ between the horizontal and vertical axes.

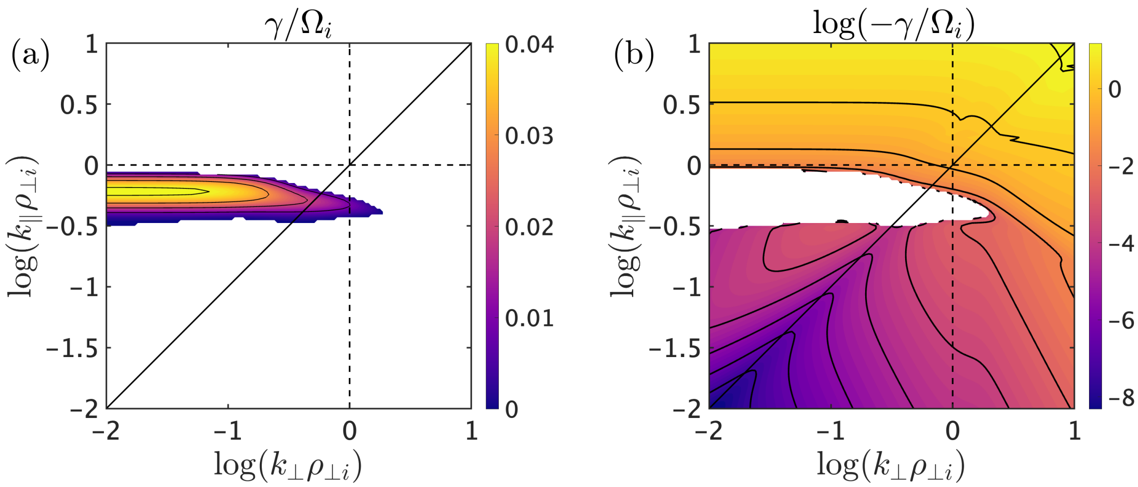

Figure S5: **Growth and Damping Rates for Alfvén/ion cyclotron wave**. (a) Linearly plotted normalized growth γ/Ω_i and (b) logarithmically plotted normalized damping rates $\log(-\gamma/\Omega_i)$ for the Alfvén/ion cyclotron wave mode as a function of $(k_\parallel \rho_{\perp i}, k_\perp \rho_{\perp i})$ for the anisotropic temperatures measured in the MMS interval under investigation.

parallel with $k_\perp \ll k_\parallel$.

The direct measurements by *MMS* in the interval under investigation show a net loss of wave energy to the ions (see Fig. 4c), manifesting collisionless damping of the measured ICWs rather than unstable growth. In kinetic theory, the real frequency of a wave mode is typically a function of the lowest order moments of the distribution (density, bulk velocity, and temperature), but the collisionless growth or damping rates can be a sensitive function of the slope of the distribution function at a resonant velocity [s4]. Furthermore, as shown by the contours of the ion velocity distribution in Fig. 2g being fit by circular contours about a parallel wave phase velocity $v_{ph} = 0.7 v_A$, the ion velocity distributions in the magnetosheath plasma may not be well approximated by the idealized bi-Maxwellian form assumed in the `PLUME` solver, leading to a difference in the resulting collisionless damping or growth rates. To determine the ion cyclotron damping rates for plasma parameters similar to the *MMS* interval studied here, we also compute the frequencies and damping rates using the `PLUME` solver by taking the ion temperatures to be isotropic, $T_{\perp i}/T_{\parallel i} = 1$, with all of the other parameters held fixed.

In Fig. 6a of the manuscript, we plot a comparison of the normalized ICW frequencies ω/Ω_i for the isotropic (dotted) and anisotropic (dashed) ion temperature cases vs. $k_\parallel d_i$; it is clear that the temperature anisotropy leads to only a relatively small (less than a factor of two) quantitative change in the wave frequency at $k_\parallel d_i > 0.3$. This supports the notion that the real frequency of the wave mode is less sensitive to the details of the velocity distribution.

In Fig. 6b of the manuscript, we plot the normalized damping rate $-\gamma/\omega$ for the isotropic case with $T_{\perp i}/T_{\parallel i} = 1$ (dotted) and the normalized damping rate $-\gamma/\omega$ (blue dashed) and normalized growth rate γ/ω (red dashed) for the anisotropic case with $T_{\perp i}/T_{\parallel i} = 2.43$. The damped regions for both cases show a similar qualitative behavior. Over the narrow parallel wavevector range $0.3 \lesssim k_\parallel d_i \lesssim 0.9$, the anisotropic case is unstable but the isotropic case is damped, with similar absolute values of the growth or damping rates. And, it is worth noting that the region of significant damping ($-\gamma/\omega > 0.1$) in the isotropic ion temperature case occurs for $k_\parallel d_i \gtrsim 0.4$, similar to the fiducial case of ion cyclotron damping explored in Sec. S1. Note also that the agreement of the damping rate at $k_\parallel d_i \lesssim 0.3$ between the isotropic and the anisotropic cases makes sense because the damping in that regime is due to Landau and transit-time damping, both of which depend only on the $\beta_{\parallel p}$, which does not change.

To assess the impact of the distribution function not being well fit by a bi-Maxwellian distribution (as assumed by the `PLUME` solver), we also calculate the linear dispersion relation via a numerical integration using the Arbitrary Linear Plasma Solver (`ALPS`) [s5], which determines complex linear wave eigenfrequencies for arbitrary gyrotropic equilibrium velocity distributions. The growth rates to these solutions are shown in Fig. S6. As inputs to this calculation, we averaged the observed ion distribution function over the entire 77 second interval considered in the manuscript, as well as shorter averaging intervals of 7 seconds and 1 second. The observed distributions are interpolated onto a Cartesian grid in $(v_\perp/v_A, v_\parallel/v_A)$ using a smooth-plate interpolation method covering a range of $v_\parallel \in [-3, 3]v_A$ and $v_\perp \in [0, 3]v_A$. We calculated the parallel propagating solutions for the Alfvén/ion cyclotron mode, keeping $k_\perp d_i = 10^{-3}$ constant with varying $k_\parallel d_i$. The forward and backwards solutions are considered separately, as asymmetries in the distribution lead to different behaviors for the two modes.

For the 77 second averaged distribution, the forward Alfvén solution remains broadly unstable (similar to the `PLUME` results), while the region of wavevector support for the backwards solution is decreased, as is the peak growth rate. When considering the shorter intervals, we see significant variability in the wavemodes that are unstable, at times nearly suppressing the instability altogether. The decrease of the instability growth rates for shorter measurement intervals is strong evidence that measured intervals yield a larger perpendicular "apparent temperature" than actually exists in the plasma [s5]. The instrumental effect of "apparent temperature" arises when wave activity, which leads to significant plasma wave motions perpendicular to the magnetic field, as is the case for both Alfvén and ion cyclotron waves, artificially broadens the measured velocity distribution. This may be an explanation for why linear dispersion relation calculations suggest that the ion cyclotron waves are unstable for this interval, but that the direct field-particle correlation measurements show instead a transfer of energy from the waves to the ions, leading to wave damping rather than growth.

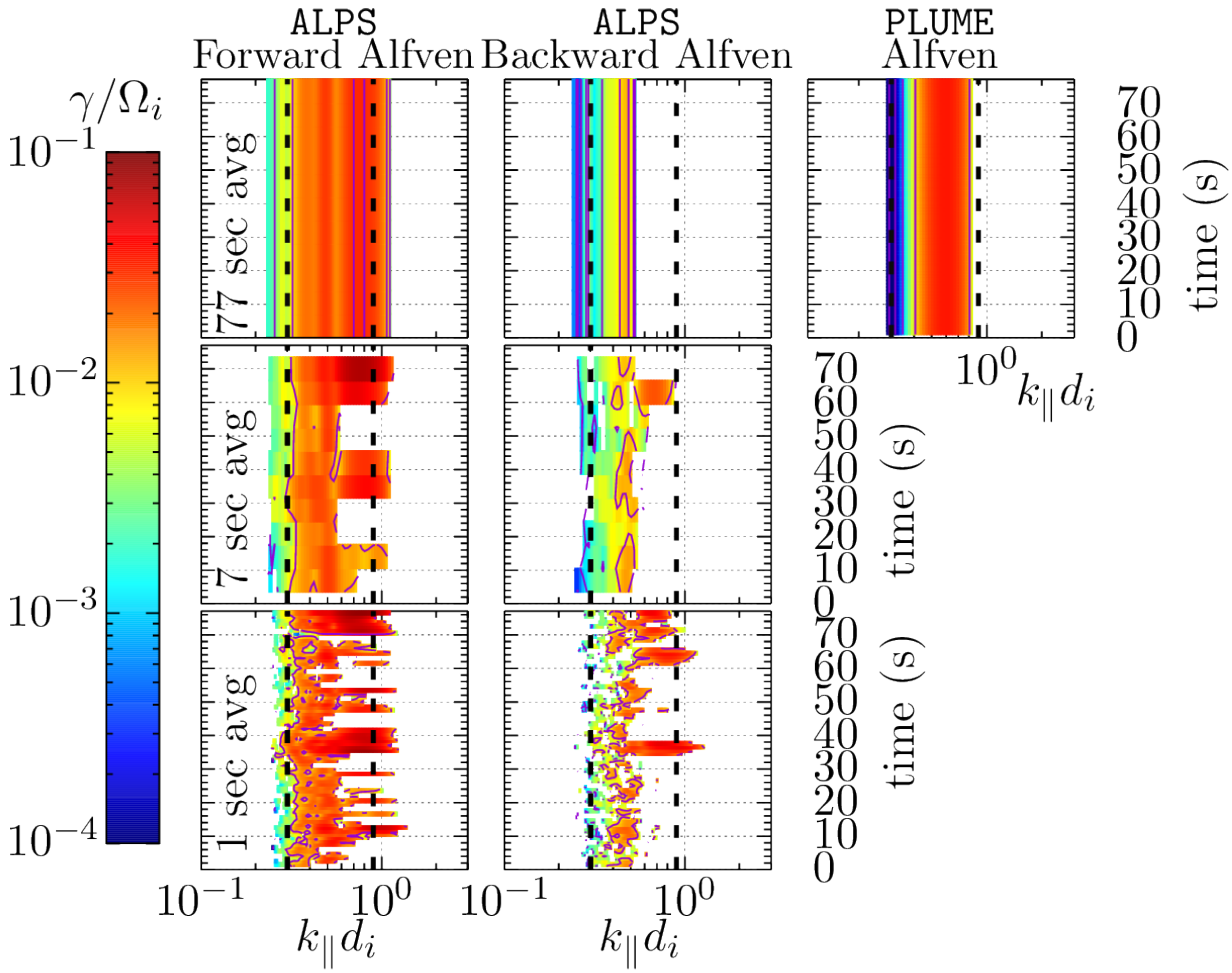

Figure S6: **Instability growth rates as a function of time average interval**. Growth rates for parallel propagating Alfvén/ion cyclotron waves as a function of $k_\parallel d_i$ and fixed $k_\perp d_i = 10^{-3}$, calculated using the PLUME bi-Maxwellian linear dispersion solver for the anisotropic temperatures presented in Fig. S5 (top right) and the ALPS linear dispersion solver (left and central columns) for three different averaging intervals (77 seconds - top, 7 seconds- middle, 1 second- bottom). The range of unstable modes identified by PLUME is overplotted as dashed lines in the other panels.

Another issue besides the apparent temperature that may impact the predictions of whether the observed ion cyclotron waves in the turbulence are damped or growing is a comparison of the unstable wave growth rates compared to the ion cyclotron wave periods themselves. For many cases of temperature anisotropy instabilities being triggered in space or astrophysical plasmas, the unstable temperature anisotropy is driven by large-scale compressible fluctuations. Because the instabilities typically grow on ion cyclotron timescales, as shown in Fig. S6, the low-frequency of the large-scale fluctuations driving the temperature anisotropy leads to a relatively steady background conditions in which the unstable wave can grow. Thus, linear dispersion relation solvers, such as `PLUME` and `ALPS`, which assume static equilibrium conditions, provide a reasonable calculation of the growth or damping rates. In this observed interval in the magnetosheath, however, the ion cyclotron wave is oscillating at $\omega/\Omega_i \simeq 0.36$, whereas the peak instability growth rates are significantly slower with $\gamma/\Omega_i \sim 0.04$. Thus, the growth or damping rates in observed turbulent plasma may not be the same as those calculated by these linear dispersion relation solvers which assume static equilibrium conditions. This is another potential explanation for why the dispersion relation solvers predict unstable wave growth, but the observations clearly indicate wave damping.

S3. Estimation of Ion Cyclotron Wave Vector

If we assume that the ICW undergoing damping in the *MMS* observation can be characterized by a single wave vector $\mathbf{k}$ (which is not unreasonable considering the appearant dominance of a single wave mode in the high-pass filtered electric and magnetic fields in Figure 2(d) and (e)), we can estimate the spacecraft frame frequency $\omega_{s/c}$ due to the sum of the plasma frame frequency plus the Doppler shift associated with the flow $\mathbf{U}$ of spatial fluctuations in the plasma past the spacecraft, given by [s6]

$$\omega_{s/c} = \omega + \mathbf{k} \cdot \mathbf{U} \tag{S4}$$

where ω is the frequency of the wave in the plasma rest frame. The FAC coordinate system defined in the Methods section is defined such that the $\hat{\mathbf{e}}_{\perp 2}$ unit vector is perpendicular to the plane of the mean magnetic field $\mathbf{B}_0$ and mean ion flow velocity $\mathbf{U}_{0i}$. Averaged over the full $\tau = 77$ s correlation interval, the mean magnetic field in GSE coordinates is $\langle B_x, B_y, B_z\rangle_\tau$ = $(14.5, 27.7, 36.2)$ nT, and the mean ion bulk flow is $\langle U_{i,x}, U_{i,y}, U_{i,z}\rangle_\tau$ =$(-51.3, -98.3, -51.8)$ km/s.

To use the measured ICW frequency $f_{ICW} = 0.26$ Hz to estimate the parallel wavenumber $k_\parallel d_i$ of the wave, we first take a single, plane-wave vector of the form

$$\mathbf{k} = k_\parallel \hat{\mathbf{e}}_\parallel + k_\perp \cos\phi \hat{\mathbf{e}}_{\perp 1} + k_\perp \sin\phi \hat{\mathbf{e}}_{\perp 2}, \tag{S5}$$

with components $k_\parallel$ and $k_\perp$ that are parallel and perpendicular to the mean magnetic field direction $\hat{\mathbf{e}}_\parallel$, and ϕ is the angle of the perpendicular component away from the $\hat{\mathbf{e}}_{\perp 1}$ direction.

With the angle between $\mathbf{B}_0$ and $\mathbf{U}_{0i}$ given by $\theta_{BU} = 156°$, substituting eq. (S5) into eq. (S4) and normalizing appropriately into dimensionless quantities, we obtain

$$\frac{\omega_{s/c}}{\Omega_i} = \frac{\omega}{\Omega_i} + (k_\parallel d_i)(U_{0i}/v_A)\cos\theta_{BU} + (k_\parallel d_i)(U_{0i}/v_A)\sin\theta_{BU}(k_\perp/k_\parallel)\cos\phi \qquad \text{(S6)}$$

Here ω/Ω_i is the real frequency from the linear Vlasov-Maxwell dispersion relation for the ICW (as shown in Fig. 6), $k_\parallel d_i$ is the independent variable, and U_{0i}/v_A and θ_{BU} are measured directly from the measurements. We must vary the unknown parameters for the perpendicular component of the wavevector $(k_\perp d_i, \phi)$, which we parameterize by the dimensionless quantities $k_\perp/k_\parallel$ and ϕ.

Since instability-driven ICWs have the most rapid growth rates with $k_\parallel \gg k_\perp$, as shown in Fig. S5, we will assume values of the wavevector anisotropy in the range $10^{-2} \leq k_\perp/k_\parallel \leq 1$. We will also allow the azimuthal angle to vary over the full range $0 \leq \phi \leq 2\pi$. Taking $U_{0i} = 122$ km/s and $v_A = 357$ km/s, we plot in Fig. S7 predictions of the normalized spacecraft-frame frequency $\omega_{s/c}/\Omega_i$ as a function of the normalized parallel wavenumber $k_\parallel d_i$. The first two terms of eq. (S6), which do not depend on the perpendicular component of the wavevector, are plotted separately, showing the plasma frame frequency ω/Ω_i (black dashed) and the Doppler-shifted parallel component of the wavevector $(k_\parallel d_i)(U_{0i}/v_A)\cos\theta_{BU}$ (red dashed). Here we take a specific value for the wave vector anisotropy $k_\perp/k_\parallel = 0.25$ and allow ϕ to vary over the full 2π. If the projection of the parallel wave phase velocity moves in the same direction as the flow, the spacecraft-frame frequency $\omega_{s/c}/\Omega_i$ is a sum of the plasma-frame frequency and parallel Doppler shift (blue solid), and the range in yellow shows how the perpendicular component changes the result with $k_\perp/k_\parallel = 0.25$ and $0 \leq \phi \leq 2\pi$. Similarly, if the parallel wave phase velocity moves in the direction opposite the flow, $\omega_{s/c}/\Omega_i$ is a difference of the plasma-frame frequency and parallel Doppler shift (green solid), with variations due to the possible variations of the perpendicular component spanned by the cyan range. The measured ICW frequency $f_{ICW} = 0.26$ Hz, when normalized to the local ion cyclotron frequency $f_{ci} = 0.73$ Hz, is indicated by the horizontal dotted line. The takeaway from Fig. S7 is that the observed ICW frequency $f_{ICW} = 0.26$ Hz can be explained by this modeling with parallel wavenumber values that span the range $0.5 \lesssim k_\parallel d_i \lesssim 1.5$ within the cyan range. This is consistent with the modeling shown in Fig. 6 of the manuscript, where damping (for the isotropic temperature case) has significant damping rates with $-\gamma/\omega > 0.1$ for values $k_\parallel d_i \gtrsim 0.6$. Therefore, we conclude that values of $k_\parallel d_i \gtrsim 0.6$ are reasonable to use to make predictions of the velocity-space signature of the ion cyclotron damping using linear Vlasov-Maxwell dispersion relation solutions.

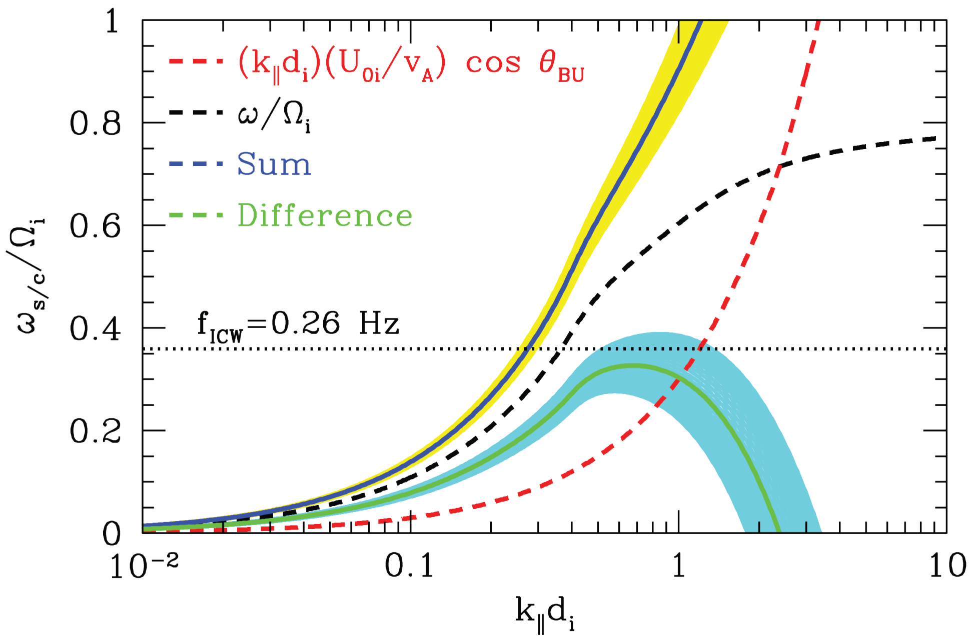

Figure S7: **Spacecraft-frame frequency of ion cyclotron wave**. Determination of the normalized spacecraft-frame frequency $\omega_{s/c}/\Omega_i$ as a function of the normalized parallel wavenumber $k_\parallel d_i$ from eq. (S6). We plot the plasma frame frequency ω/Ω_i (black dashed) and the Doppler-shifted parallel component of the wavevector $(k_\parallel d_i)(U_{0i}/v_A)\cos\theta_{BU}$ (red dashed). The sum (blue solid) and difference (green solid) of the plasma-frame frequency and parallel Doppler shift are shown. When the contribution of the perpendicular component of the wavevector with $k_\perp/k_\parallel = 0.25$ and $0 \leq \phi \leq 2\pi$ is included, the resulting possible range of spacecraft-frame frequencies $\omega_{s/c}/\Omega_i$ is given by the yellow range for the sum of the cyan range for the difference.

S4. Estimation of Upstream Bow Shock Parameters

The ICWs observed in the *MMS* interval analyzed here are most likely to have been generated by a significant ion temperature anisotropy $T_{\perp i}/T_{\parallel i} > 1$ through the Alfvén/ion cyclotron instability [s7, s8]. An obvious candidate mechanism for the generation of an ion temperature anisotropy that exceeds the threshold for this instability [s8] is compression of the incoming solar wind at Earth's bow shock. For quasiperpendicular upstream bow shock conditions $\theta_{Bn} > 45°$, one indeed expects the generation of an anisotropy in the sense of $T_\perp/T_\parallel > 1$. Therefore, it is worthwhile investigating the conditions at the bow shock to determine whether shock compression is likely to trigger the generation of the ICWs observed by *MMS* downstream in the magnetosheath.

The burst-mode interval at 07:24:28 on 12 JAN 2016 investigated here occurs on the inbound pass from apogee to perigee, but the *MMS* spacecraft unfortunately did not cross the bow shock on its previous passage through apogee, so a direct determination of the upstream conditions of the shock—in particular the Alfvén Mach number M_A and shock normal angle θ_{Bn} in the normal incidence frame—is not possible. Instead, we are forced to use the magnetic field direction upstream from an upstream solar wind monitor and the direction of the bow shock normal upstream from our measured interval to estimate the shock normal angle θ_{Bn}. In Geocentric Solar Eclicptic (GSE) coordinates, the *MMS* burst-mode interval at 7:24:28 occurs at $(9.59, -4.00, -0.97)R_E$, where the radius of the Earth is $R_E = 6378$ km. Using a model of the Earth's bow shock [s9], we estimate the bow shock crossing position as the position directly toward the Sun in the GSE x direction at $(13.36, -4.00, -0.97)R_E$, with a shock normal unit vector in GSE coordinates of $(0.986, -0.160, -0.039)$. During this time, the *ACE* spacecraft was monitoring the upstream solar wind conditions at the L1 point with a position $(235.17, 0, 0)R_E$. The solar wind velocity measured at *ACE* in the hour before the *MMS* measurements is fairly steady at approximately 600 km/s, and the solar wind flow velocity in the magnetosheath downstream of the bow shock measured during the *MMS* interval is 112 km/s. Together, the travel time for the solar wind plasma to flow from *ACE* through the bow shock to the position of *MMS* is estimated to be 42.6 min. Making the assumption the direction of the magnetic field (frozen into the solar wind flow) does not change from the position of *ACE* to the bow shock, using the magnetic field direction at *ACE* at time 06:41:52, we obtain a shock-normal angle of $\theta_{Bn} = 15^\circ \pm 7^\circ$, where the standard deviation is taken over a four minute interval centered at that time. This estimate puts the upstream conditions of the shock into the regime of quasiparallel shocks with $\theta_{Bn} < 45^\circ$, seemingly in contradiction with the need for a more perpendicular shock crossing to lead to the measurements of $T_{\perp i}/T_{\parallel i} > 1$.

Of course, estimating the local direction of the magnetic field at the bow shock crossing upstream of our measured *MMS* interval in the magnetosheath using data from the *ACE* spacecraft at position $235.17R_E$ and at a time 42.6 min earlier carries significant uncertainties. In addition, quasiparallel shocks at sufficiently high Mach numbers lead to significant upstream perturbations that can lead to large local changes of the magnetic field direction at the shock crossing [s10, s11, s12]. The ACE data give an upstream magnetic field magnitude of $|\mathbf{B}| \sim 6$ nT and we estimate the upstream proton number density of $n_i \sim 2$ cm^{-3}, so the Alfvén velocity is $v_A = 93$ km/s, leading to an Alfvén Mach number of $M_A \sim 6.4$. At this supercritical Mach number [s13], particle reflection at the shock can indeed lead to significant upstream fluctuations, so the local shock normal angle θ_{Bn} upstream of the measured *MMS* interval could possibly have had a much larger $\theta_{Bn} > 45^\circ$, leading to the local generation of the sufficiently large ion temperature anisotropy $T_{\perp i}/T_{\parallel i} > 1$ to generate the ICWs that were observed. Though we do not have any clear confirmation of conditions that we expect would generate such a perpendicular temperature anisotropy, we cannot rule out such upstream conditions at the shock.

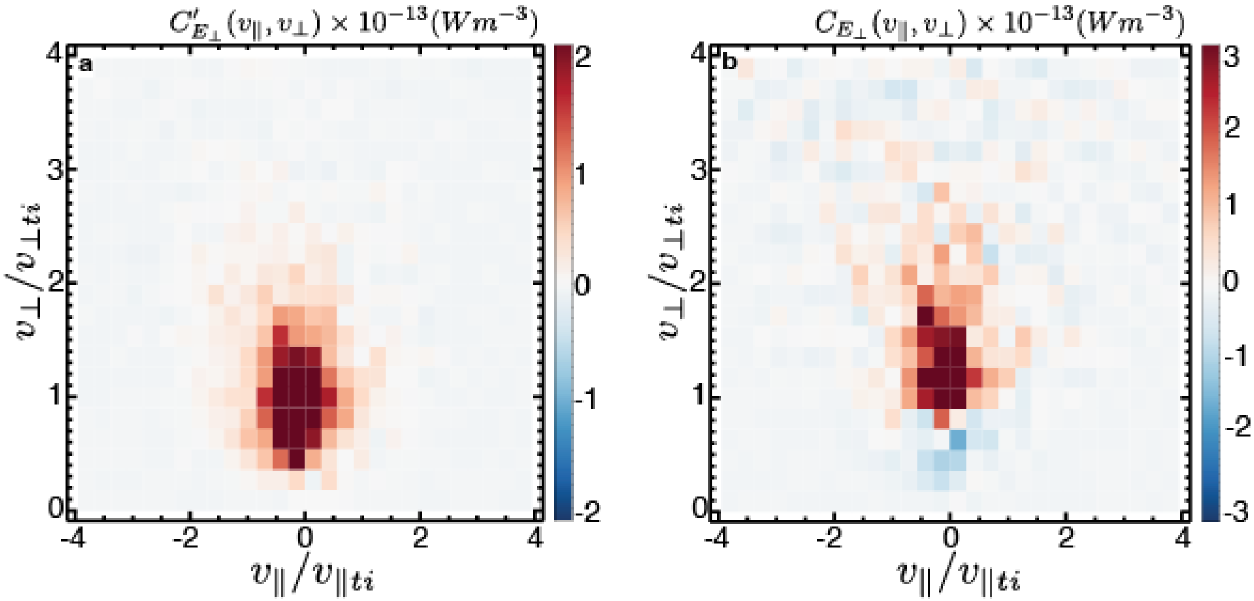

Figure S8: **Standard vs. alternative field-particle correlation**. **a** Alternative field-particle correlation $C'_{E_\perp}(v_\parallel, v_\perp; \tau)$ and **b** field-particle correlation $C_{E_\perp}(v_\parallel, v_\perp; \tau)$ shown for $\tau = 77$ s.

S5. Observation of 2V Gyrotropic $C'_{E_\perp}(v_\parallel, v_\perp)$ and $C_{E_\perp}(v_\parallel, v_\perp)$

The intermediate step in the computation of the field-particle correlation $C_{E_\perp}(v_\parallel, v_\perp)$ is the computation of the alternative field-particle correlation $C'_{E_\perp}(v_\parallel, v_\perp)$ using Eq. 5 of the manuscript. In Fig. S8a we show $C'_{E_\perp}(v_\parallel, v_\perp)$ and in Fig. S8b we show $C_{E_\perp}(v_\parallel, v_\perp)$.

S6. Collisionless Damping Rates for the Anisotropic Turbulent Cascade

In Fig. S9, we plot (a) the normalized frequency $\omega / k_\parallel v_A$ and (b) the normalized collisionless damping rate $-\gamma/\omega$ for the anisotropic fluctuations ($k_\perp \gg k_\parallel$) of the large-scale turbulent cascade over the range at $10^{-2} \leq k_\perp \rho_{\perp i} \leq 10^2$ for $k_\parallel \rho_{\perp i} = 10^-3$ with the plasma parameters $\beta_{\parallel i} = 0.383$, $T_{\parallel i}/T_{\parallel e} = 6.84$, $T_{\perp e}/T_{\parallel e} = 0.973$, $v_{\parallel ti}/c = 7.34 \times 10^{-4}$, and with dashed lines corresponding to $T_{\perp i}/T_{\parallel i} = 2.43$ and solid lines corresponding to $T_{\perp i}/T_{\parallel i} = 1$. Note that, in the limit $k_\perp \gg k_\parallel$ that is relevant to the fluctuations of the large-scale turbulent cascade, the normalized damping rate $-\gamma/\omega$ is independent of the value of $k_\parallel$ as long as $k_\parallel d_i \lesssim 1$. In Fig. S9(b), the total normalized damping rate $-\gamma/\omega$ (black) is decomposed into ion $-\gamma_i/\omega$ (red) and electron $-\gamma_e/\omega$ (blue) contributions, both of which are dominated by collisionless damping via the Landau resonance for these plasma parameters. The critical finding here is that collisionless damping via the Landau resonance for the ions is very weak, with $-\gamma/\omega \lesssim 4 \times 10^{-3}$, due to the fact that the low $\beta_{\parallel i} = 0.383$ leads to a parallel phase velocity for Alfvén waves that falls in the tail of the ion velocity distribution.

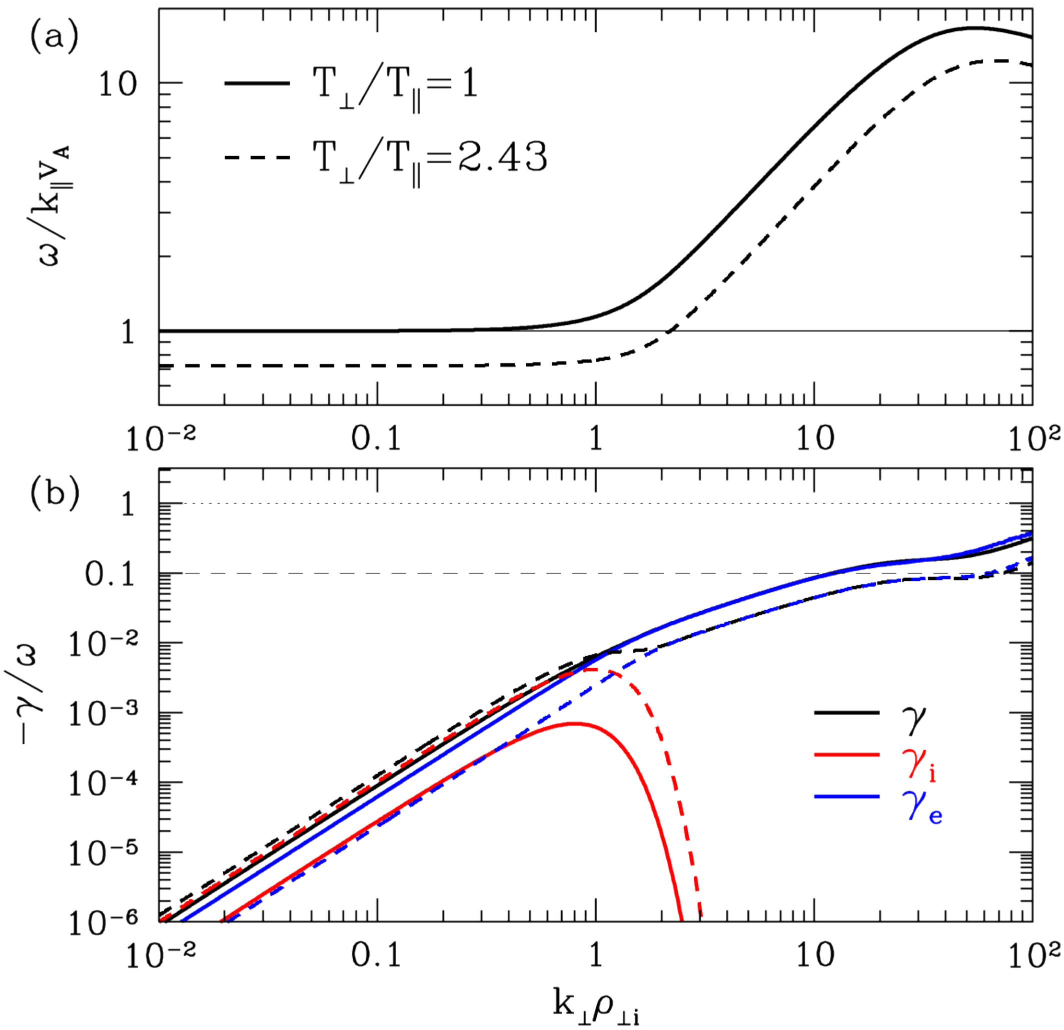

Figure S9: **Alfvén wave frequency and damping rate**. From the linear dispersion relation for Alfvén waves, (a) the normalized frequency $\omega/k_\parallel v_A$ and (b) the normalized collisionless damping rate $-\gamma/\omega$ for the parameters of the large-scale cascade with a typical wavevector anisotropy $k_\perp \gg k_\parallel$. In this limit, ion damping is dominated by the Landau resonance (Landau and transit-time damping), and the ion contribution to the normalized damping rate γ_i/ω is given by the red curves for $T_{\perp i}/T_{\parallel i} = 1$ (solid) and $T_{\perp i}/T_{\parallel i} = 2.43$ (dashed). Significant collisionless damping occurs when $-\gamma_i/\omega \gtrsim 0.1$, but here the maximum damping rates for ions have $\gamma_i/\omega \lesssim 4 \times 10^{-3}$, yielding very weak ion damping.

References

[s1] Klein, K. G. & Howes, G. G. Predicted impacts of proton temperature anisotropy on solar wind turbulence. *Phys. Plasmas* **22**, 032903 (2015). `1503.00695`.

[s2] Kunz, M. W., Schekochihin, A. A., Chen, C. H. K., Abel, I. G. & Cowley, S. C. Inertial-range kinetic turbulence in pressure-anisotropic astrophysical plasmas. *J. Plasma Phys.* **81**, 325810501 (2015). `1501.06771`.

[s3] Squire, J. *et al.* High-frequency heating of the solar wind triggered by low-frequency turbulence. *Nature Astron.* **6**, 715–723 (2022). `2109.03255`.

[s4] Walters, J. *et al.* The effects of nonequilibrium velocity distributions on alfvén ion-cyclotron waves in the solar wind. *Astrophys. J.* **955**, 97 (2023). URL `https://dx.doi.org/10.3847/1538-4357/acf1fa`.

[s5] Verscharen, D. *et al.* ALPS: the Arbitrary Linear Plasma Solver. *J. Plasma Phys.* **84**, 905840403 (2018). `1803.04697`.

[s6] Howes, G. G., Klein, K. G. & TenBarge, J. M. Validity of the Taylor Hypothesis for Linear Kinetic Waves in the Weakly Collisional Solar Wind. *Astrophys. J.* **789**, 106 (2014). `1405.5460`.

[s7] Gary, S. P., Montgomery, M. D., Feldman, W. C. & Forslund, D. W. Proton temperature anisotropy instabilities in the solar wind. *J. Geophys. Res.* **81**, 1241–1246 (1976).

[s8] Hellinger, P., Trávníček, P., Kasper, J. C. & Lazarus, A. J. Solar wind proton temperature anisotropy: Linear theory and WIND/SWE observations. *Geophys. Res. Lett.* **33**, 9101–+ (2006).

[s9] Farris, M. H., Russell, C. T. & Thomsen, M. F. Magnetic structure of the low beta, quasi-perpendicular shock. *J. Geophys. Res.* **98**, 15285–15294 (1993).

[s10] Schwartz, S. J. *et al.* Observations of short large-amplitude magnetic structures at a quasi-parallel shock. *J. Geophys. Res.* **97**, 4209–4227 (1992).

[s11] Lucek, E. A., Horbury, T. S., Dandouras, I. & Rème, H. Cluster observations of the Earth's quasi-parallel bow shock. *J. Geophys. Res.* **113**, 7 (2008).

[s12] Caprioli, D. & Spitkovsky, A. Simulations of Ion Acceleration at Non-relativistic Shocks. I. Acceleration Efficiency. *Astrophys. J.* **783**, 91 (2014). `1310.2943`.

[s13] Kennel, C. F. Critical Mach numbers in classical magnetohydrodynamics. *J. Geophys. Res.* **92**, 13427–13437 (1987).